

Landslides (2019) 16:1003–1020
 DOI 10.1007/s10346-019-01159-x
 Received: 3 January 2019
 Accepted: 20 February 2019
 Published online: 5 March 2019
 © Springer-Verlag GmbH Germany
 part of Springer Nature 2019

Xuanmei Fan · Qiang Xu · Andres Alonso-Rodriguez · Srikrishnan Siva Subramanian · Weile Li · Guang Zheng · Xiujun Dong · Runqiu Huang

Successive landsliding and damming of the Jinsha River in eastern Tibet, China: prime investigation, early warning, and emergency response

Abstract Two successive landslides within a month started in October 11, 2018, and dammed twice the Jinsha River at the border between Sichuan Province and Tibet in China. Both events had potential to cause catastrophic flooding that would have disrupted lives of millions and induced significant economic losses. Fortunately, prompt action by local authorities supported by the deployment of a real-time landslide early warning system allowed for quick and safe construction of a spillway to drain the dammed lake. It averted the worst scenario without loss of life and property at least one order of magnitude less to what would have been observed without quick intervention. Particularly, the early warning system was able to predict the second large-scale slope failure 24 h in advance, along with minor rock falls during the spillway construction, avoiding false alerts. This paper presents the main characteristics of both slope collapses and damming processes, and introduces the successful landslide early warning system. Furthermore, we found that the slope endured cumulative creeping displacements of > 40 m in the past decade before the first event. Twenty-five meter displacement occurred in the year immediately before. The deformation was measured by the visual interpretation of multitemporal satellite images, which agrees with the interferometry synthetic aperture radar (InSAR) measurement. If these had been done before the emergency, economic losses could have been reduced further. Therefore, our findings strengthen the case for the deployment of systematic monitoring of potential landslide sites by integrating earth observation methods (i.e., multitemporal satellite or UAV images) and in situ monitoring system as a way to reduce risk. It is expected that this success story can be replicated worldwide, contributing to make our society more resilient to landslide events.

Keywords Successive landslides · Landslide dam · Potential geohazards · Long term deformation · Monitoring and early warning · Emergency response

Introduction

On October 11, 2018, a large landslide occurred on the west bank of the Jinsha River near Baige Village, Jiangda County, Tibet, People's Republic of China (31° 4' 59.62" N, 98° 42' 30.8" E). Large rock masses moved downslope reaching the bottom of the valley, blocking the Jinsha River and impounding a 290 million m³ lake. On October 12, 2018, the dammed lake started draining naturally, ending in a breach on October 13 and minor flooding as a consequence. On November 3, 2018, the landslide reactivated again triggering a large rock avalanche that dammed the river for a second time and formed a new barrier lake. Constant inflow from upstream made the barrier lake swell to 524 million m³ on November 12, flooding the town of Bolo, Tibet (Peteley 2018). First response to this emergency resulted in evacuation of 25,000 people by the state councils of Sichuan and Tibet in China.

The successive landslides occurred in a tectonically active and fragile geologic region in steep mountainous terrains of Eastern Tibet in Southwest China. Due to significant crustal uplift of the Qinghai-Tibet plateau, there is strong and rapid incision of rivers, resulting in widespread large-scale destabilization of slopes along both sides of valleys (Huang 2012; Liu et al. 2013; Ren et al. 2017; Fan et al. 2018b). Furthermore, the geological setting in this area is complex, characterized by high geo-stresses, high seismic activity, and strong weathering, causing large landslides that often lead to landslide dams. Along the Jinsha River and its tributaries, 61 ancient landslides and the consequent river damming events have been recorded (Chai et al. 2000; Sijing et al. 2010).

The emergency response team of the Sichuan Land and Resources Department, together with our research team from the State Key Laboratory of Geohazard Prevention and Geoenvironment Protection (SKLGP) of China, quickly carried out detailed field investigation and topographic analysis of the landslide using an unmanned aerial vehicle (UAV). Cracks and potential failure paths were identified on top of the ridge over the valley. This outcome justified deployment of a real-time monitoring system comprised of more than 16 sets of global navigation satellite system (GNSS) monitoring stations, 16 crack gauges, and a rainfall monitoring station. Field measurements were carried over as input to a near real-time landslide early warning model developed by SKLGP (Huang et al. 2013, 2015) with the aim of predicting and mitigating secondary hazards.

As the volume of the lake formed by the second failure was increasing quickly and potential uncontrolled collapse of the landslide dam could lead to catastrophic flooding disrupting the lives of millions downstream, authorities decided to construct an artificial spillway, as it was done before in other events to reduce effects of river damming (Fan et al. 2012a, b and c). Once results from the early warning system showed that the site was stable enough to warrant reasonable chances of a successful outcome, the construction of a spillway began and was completed on November 13. Important flooding was observed in the aftermath. However, loss of life was completely averted and economic loss was orders of magnitude less than what would have happened under a catastrophic uncontrolled breach.

This case shows the advantages in risk mitigation by setting up an effective early warning system through integrating field monitoring, remote sensing, and real-time predictive modeling. Good practices in the aftermath of the Baige landslide add to recent experiences, for example, the Xinmo Landslide in Sichuan China on June 24, 2017 (Fan et al. 2017, 2018a). Thus, widespread application of a framework for integrating remote sensing, early warning system, and secondary hazard assessment is recommended worldwide to make our society more resilient to landslide hazard.

Geological background

The landslide developed along a ridge at the west bank of the Jinsha River striking 10° N– 15° E with a dip direction of 80° – 100° over a “V”-shaped valley, from an elevation of 3720 m a.s.l. down to 2880 m a.s.l. A three-dimensional view of the site is shown in Fig. 1. Strong neotectonism has been observed accompanied by various geologic hazards along the Jinsha River, which runs across the Hengduanshan north-south tectonic zone (Wang et al. 2000). The monsoonal climate of the Eastern Tibetan Plateau influences the microclimate of the area, which shows an annual precipitation and temperature of 627 mm/year and 8.0° C, respectively, including 3 to 4 months of freezing.

The exposed rock outcrops near the source area are shown in Fig. 2. The main source rock of the landslide was found to be serpentinite. On the southern side of the landslide body, gneiss rock was exposed around 3450 m (Fig. 2a) and behind the landslide scarp along the road (Fig. 2b). Further, gray gneiss outcrops were found adjacent to the landslide body on southern side (Fig. 2c). On the northern side of the landslide body, at the back scarp, green-white colored crushed serpentinite outcropped as shown in Fig. 2d.

The strata outcropping in the area belong to the Jingu (Ji), Xianisongduo (Xi1), Shengpa (Sh), and Xionsong (Xi2) formations of Upper Triassic, Upper Carboniferous, and Upper Ordovician periods (Fig. 3). They mainly consist of gneiss (P_{gneiss}), granite ($\gamma\delta_5^{2d}$), limestone (T_3jn), and serpentinite (ϕ_{w4}). The landslide headscarp was developed within the serpentinite from Variscan orogeny. The landslide body is mainly composed of gneiss and serpentinite (Fig. 2). The attitude of the gneiss strata is $235^{\circ}\angle 40^{\circ}$. They are crossed by two groups of structural planes dipping 60° – $80^{\circ}\angle 75^{\circ}$ – 85° and 100° – $115^{\circ}\angle 80^{\circ}$, respectively.

The tectonic setting is conditioned by several structures striking in the NW direction; significant among them are the Bolou-

Muxie (F4), Zhuying-Gonda (F2), Xuenqing-Longgang (F1) faults, and the Shandong-Baba Anticline (M1). The landslide is located at the west bank of the Jinsha River right on the edge of the Bolou-Muxie fault (F4). Thus, a 300-m-wide band of crushed rock consisting of gneiss and serpentinite makes it prone to landsliding.

Large crustal earthquakes have occurred in the Jinsha River area at the border between Sichuan Province and Tibet. Particularly, the 1842 M_w 7.3 Zongguo earthquake, the 1870 M_w 7.2 Batang earthquake, and the 1989 M_w 6.5 earthquake (Zinun 1995; Ambraseys and Douglas 2004) are worth mentioning as their epicenters were less than 125 km downstream and upstream from the location of the Baige landslide. However, there are no reports of large earthquakes (M_w 6.0) within the past 100 years according to the ISC-GEM catalog (Storchak et al. 2013) at a distance of 50 km from the landslide; likewise, the only one moderate magnitude event ($M_w > 4.5$) was recorded in the past 20 years, 40 km away from the site (USGS 2018). Therefore, it is highly unlikely that significant strains and stresses induced by earthquake ground motion in past decades played a role in formation of the Baige landslide events.

Estimates of long-term fault displacement rates within the study area are not available. However, to our best knowledge, the long-term steady-state creep may lead to extensive cracking and sliding in an aseismic context, making slopes prone to landsliding. Moreover, the Bolou-Muxie fault is part of a 180-km-long continuous section of the Jinsha River Thrust system that could lead to earthquakes up to M_w 8.2 if it ruptures completely (Wells and Coppersmith 1994). If that happens, extensive and more severe damming of the Jinsha River is possible. Consequently, there is a need for deep assessment of the tectonic setting, considering effects of potential earthquakes on landslide hazard at a regional scale, with continuous monitoring of the Jinsha River Canyon.

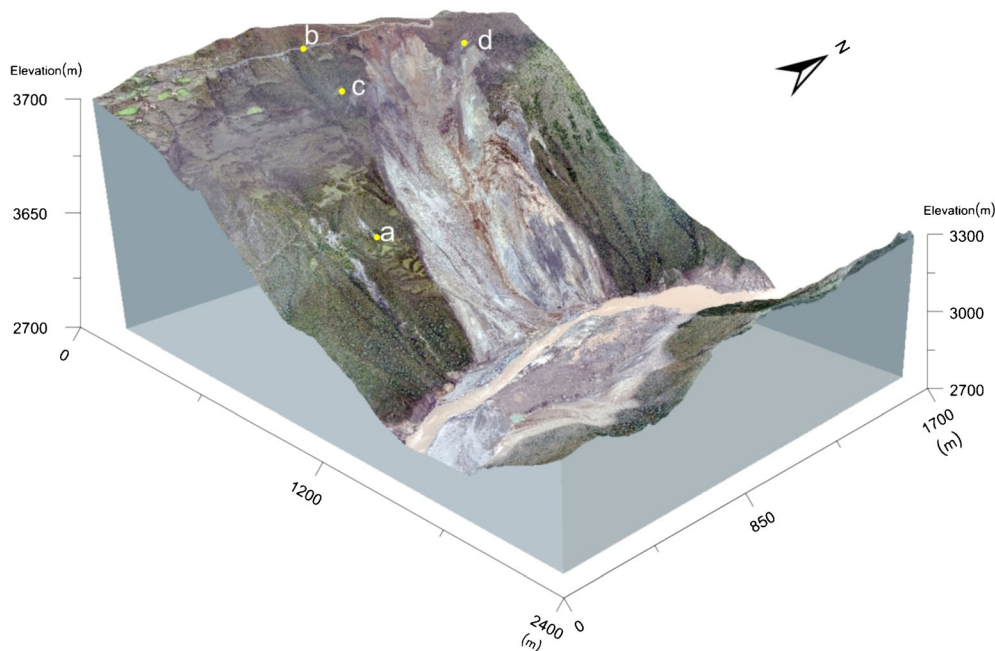


Fig. 1 Three-dimensional view of the October 11, 2018, landslide. The points shown a, b, c and d are locations of the photographs taken during field investigation (see Fig. 2)

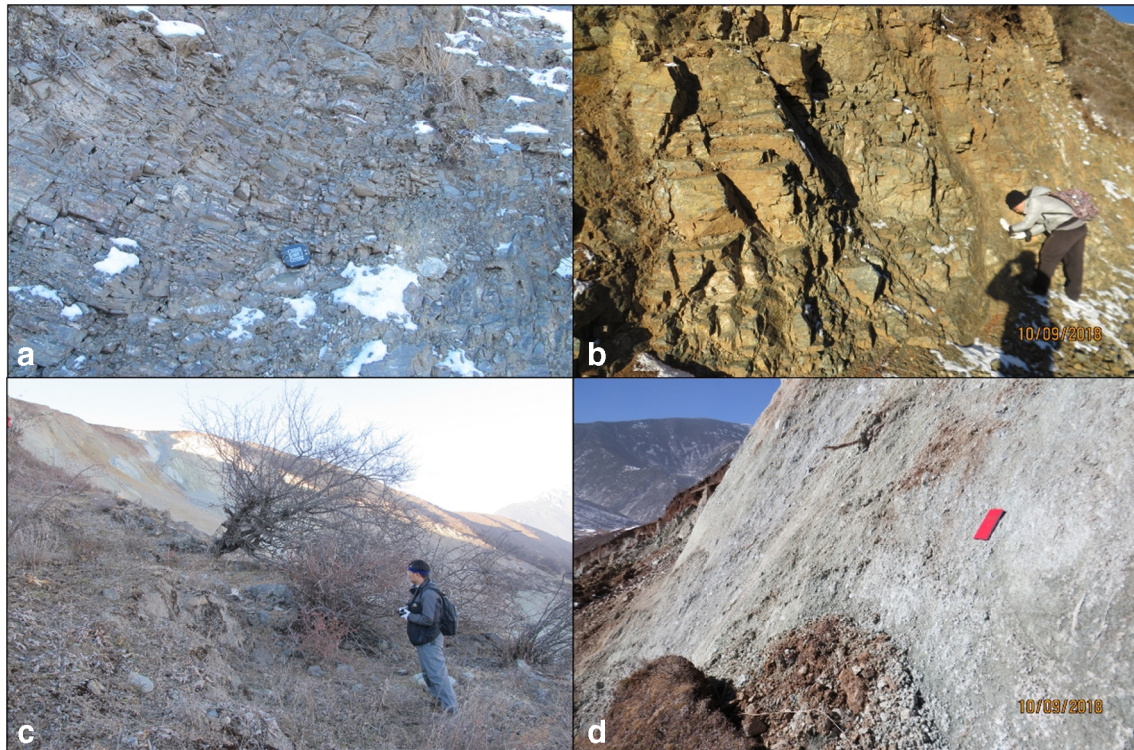


Fig. 2 Exposed rock outcrops around the main landslide area. **a** Gneiss outcropped near 3450 m southern side. **b** Gneiss outcropped along the road at the top of the landslide. **c** Gray gneiss outcropped adjacent to the landslide on southern side. **d** Green-white crushed serpentinite outcropped on the back scarp of the landslide

Data and methods

This study presents a detailed collection of data from diverse sources, obtained before, during and after the emergency, allowing for a wide-reaching and coherent panorama of each of the single events observed and their potential cascading consequences. A summary is presented in Table 1 and Fig. 4.

Visual interpretation of the landslide evolution through multitemporal satellite images having optimal ground resolution has been proven to be helpful in identifying macroscopic deformation indicators, mostly cracks and other major discontinuities (e.g., Zhang et al. 2013; Tian et al. 2017; Fan et al. 2017; Stumpf et al. 2017; Wu et al. 2017; Türk 2018). In order to analyze these deformation trends, in this study, 15 satellite images (see Table 1 for details) taken since 1966 were sourced, analyzed, and interpreted in a GIS framework (ArcGIS) to track the deformation history of the landslide (see “Deformation history of the landslide revealed by remote sensing data” section).

Likewise, unmanned aerial vehicles (UAV) are a valuable resource for landslide disaster and emergency response, as a tool to immediately investigate and map potential unstable zones to predict secondary hazards (Turner et al. 2015; Peterman 2015; Fan et al. 2017; Fan et al. 2018b). A Pegasus F-1000 fixed-wing UAV made by Feima Robotics was deployed to obtain high-resolution images with a resolution of 10–15 cm, digital surface models (DSMs), and digital orthophoto maps (DOMs) of the site. Furthermore, the DSM taken after the first landslide was compared with a 1:10,000 pre-sliding DEM sourced from the Sichuan Bureau of Surveying and Mapping to estimate the depth and volume of the first failure. Using the pre-sliding Gaofen-2 image (taken on

August 9, 2018) and comparing with the post-sliding UAV data, detailed geomorphological characteristics of both landslide events on October 11 and November 3 have been analyzed (see “Characteristics of both landslide events” section). Time constrains prevented setup of ground control points for improving the precision of both DOM and DSM.

In recent decades, remote sensing-based deformation monitoring/prediction and advanced processing of synthetic aperture radar (SAR) images have been widely used for landslide detection and mapping (Farina et al. 2006; Cascini et al. 2009; Guzzetti et al. 2009; Monserrat et al. 2014; Schlägel et al. 2015). In this study, we estimated displacements at a grid of points on the landslide surface using four scenes of ALOS PalsAR-2 radar satellite data from July 2017 to July 2018.

As consequence of the first event on October 11, we deployed a real-time landslide monitoring system network comprised by 16 sets of global navigation satellite system (GNSS)-based displacement sensors, 16 crack gauges, and 1 rainfall gauge at the crown of the landslide (see “Emergency rescue operation, monitoring, and early warning system” section). When a second slope failure was observed, some of the sensors were damaged. However, the network remained operative, ensuring the safety of the spillway construction. Monitoring data was processed and input into an early warning model developed by SKLGP (Huang et al. 2013, 2015).

Deformation history of the landslide revealed by remote sensing data

The visual interpretation of historical satellite images shows that the site has experienced creep deformation in the last 50 years. Image taken in 1966 reveals tensile cracks and slight surface

Recent Landslides

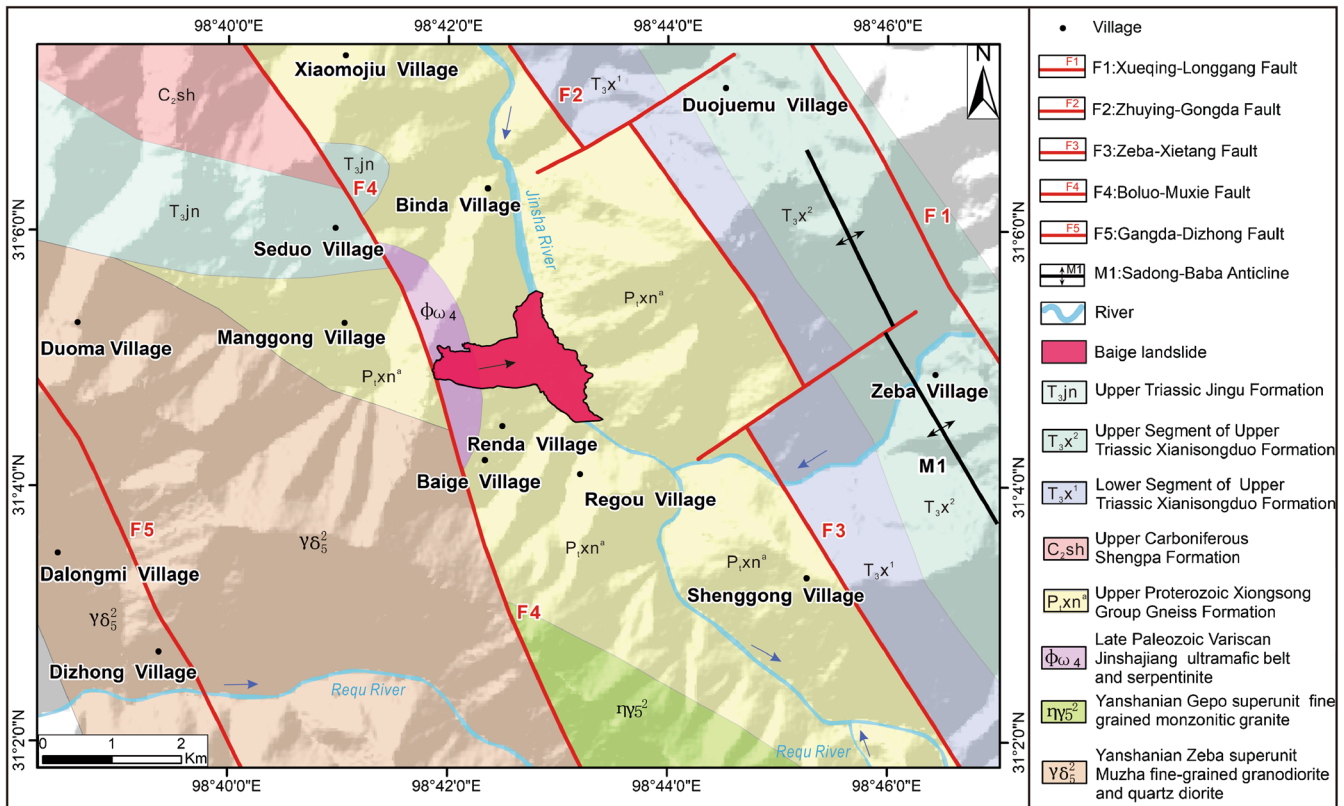


Fig. 3 Geological map of the investigated area

disruption as shown in Fig. 5a. The slope might have been already gravitationally deforming and prone to failure. In 2011, a continuous tensile crack had formed at the back scarp while surface disruption increased as shown in Fig. 5b. Overall deformation of the slope might have begun in 2011. Satellite images taken in March 2011 and in November 2015 (Fig. 5c) reveal how extensive cracking at the scarp had led to a dislocation. The deformation over the body of the creeping mass continued increasing during 2017 and 2018 (see Fig. 5d, e). Images taken in 2018 reveal how these trends accelerated, leading to a formation of a shear zone at the lower and middle sections of the moving mass. Finally, the image taken on August 2018 (in Fig. 5f) shows extensive disruption and signs of further deformation, indicating that the landslide was in an equilibrium state close to instability. Therefore, catastrophic failure of the slope was imminent.

Quantitative assessments of these deformation processes can be done by tracking displacements of highly reflective locations along time. Roads are particularly helpful for that purpose. Our analysis in Fig. 6 shows that the maximum horizontal displacement of the creeping landslide reached 47 m since 2011, increasing by 26 m between 2017 and 2018.

Displacement estimates were validated by the interferometry synthetic aperture radar (InSAR) measurement through pixel offset tracking. It can be seen that maximum displacement on satellite line of sight (LOS) direction within the landslide body reached 25 m from July 2017 to July 2018 (Fig. 7), in agreement with what was obtained from multispectral images (Figs. 5 and 6).

Thus, the historical deformation observed by remote sensing data shows how the slope was deformed through a process of steady movement for decades, prior to the first failure on October 11, 2018. Also, it demonstrates how rock fracturing and acceleration of displacements were developed on the whole creeping body a year before collapse. Our analysis also shows how it is possible to employ remote sensing techniques directly to monitor deformation of unstable slopes. If continuous monitoring of the canyon of the Jinsha River had been in place, it would have been possible to utilize detailed numerical models, adopt system response protocols, and even perform mitigation works that could have reduced economic fallout further.

Characteristics of both landslide events

Overview of both events

On October 11, a crack at 3000 m a.s.l. opened and eventually led to collapse, involving 23 million m³ of rock mass and debris that blocked the Jinsha River at 2850 m a.s.l. Some of the landslide deposits run up to the other bank of the river reaching an elevation of 2950 m a.s.l. (Fig. 8). The landslide dam started breaching naturally the next day. Fortunately, the lake was relatively small (290 million m³); therefore, by October 13, it had already drained without causing loss of life and significant property damage.

On November 3, a second slope failure was developed at the scarp of the previous landslide. This time 3.5 million m³ of the rock mass detached from elevations ranging 3000 to 3800 m a.s.l. The source mass entrained 8.5 million m³ of deposits from the previous landslide, finally blocking the Jinsha River again. However, natural

Table 1 Summary of data considered in this study

Data	Resolution	Date	Source
Before disaster			
Topographic map	1:10,000		Sichuan Bureau of Surveying Mapping and Geoinformation
Geologic map	1:200,000		
KeyHole image	2.7 m	1966.02.08	KeyHole KH-4A Satellite
GeoEye-1 image	0.41 m	2011.03.04	Digital Globe
Ziyuan ZY-3 image	2.1 m	2014.01.08	China National Space Administration
Ziyuan ZY-3 image	2.1 m	2014.12.28	China National Space Administration
GeoEye-1 image	0.41 m	2015.02.22	Digital Globe
Gaofen-1 GF-1 image	2.0 m	2015.08.10	Chinese satellite Gaofen-1
Ziyuan ZY-3 image	2.0 m	2015.11.13	China National Space Administration
Ziyuan ZY-3 image	2.1 m	2016.01.06	China National Space Administration
Gaofen-1 GF-1 image	2.0 m	2016.05.23	Chinese satellite Gaofen-1
Gaofen-2 GF-2 image	0.8 m	2017.01.15	Chinese satellite Gaofen-2
Gaofen-2 GF-2 image	0.8 m	2017.08.05	Chinese satellite Gaofen-2
Gaofen-2 GF-2 image	0.8 m	2017.10.18	Chinese satellite Gaofen-2
Gaofen-2 GF-2 image	0.8 m	2017.12.21	Chinese satellite Gaofen-2
Gaofen-2 GF-2 image	0.8 m	2018.02.28	Chinese satellite Gaofen-2
PlanetScope	3.0 m	2018.08.29	
InSAR		2017.07.27–2018.07.23	ALOS-2 SAR image
After disaster			
UAV images	0.15 m	2018.10.12	SKLGP
		2018.10.23	
		2018.11.05	

breaching of this new landslide dam was not observed even 5 days after its formation, impounding a 524 million m³ barrier lake. This could have been a consequence of further compaction due to high velocity impact, increasing its relative density and consequently making it less prone to erosion. By November 8, the overall water level was steadily rising in such way that catastrophic collapse of the dam was possible.

Thus, it was decided to start excavation of a spillway to reduce the risk of potential dam-breach flood. The construction of the spillway was completed on November 12 and the lake started to drain on November 13. A geological cross section of both landslides (Fig. 9) shows that the main landslide body consists of serpentinite from the upper part of the slope and of gneiss from its lower part. Through comparing the pre-sliding and post-sliding topographies of October 11 and November 3 events (Fig. 9), it is visible that the failure on November 3 deepened more over the serpentinite rock. The overall height of the first landslide dam from the bottom of the river was estimated as 85 m. The lake water level was around 50 m. The natural breaching of the first landslide dam could be attributed to the loose materials deposited over relatively low elevation and its U-type morphology (see Fig. 9). The landslide dam body formed after the November 3 event was estimated over 135 m high, comparatively higher than the maximal height of the October 11 event, which made the dam relatively stable for slightly longer period due to enhanced material compaction.

Characteristics of first slope collapse

By comparing the pre- and post-sliding DEMs, it can be seen that the first failure started between 3000 and 3500 m a.s.l. This material loss carved a depression of 90 m in the scarp of the source area (I) as shown in Fig. 8. Material moved downslope until reaching 2800 m a.s.l. at the bottom of the canyon, confirming a clear transportation (II) and deposition area (III) that dammed the river. Furthermore, a portion of it surged uphill on the other bank (IV). Disruption induced by the landslide led to instability at the rear and lateral margins of the landslide source area (K₁, K₂, and K₃ as indicated in Fig. 8).

(1) Landslide source area (I)>

Field investigation revealed that serpentinite belts are predominant in the upper and middle parts of the source area. They are crystallized at the top, appearing a dark green color. Lower belts, 300 m thick, are in gray and pale green colors instead, indicating presence of chlorite. The middle and lower parts of the source area are comprised of moderately weathered gneiss with an attitude of 235°∠40°. The landslide source is bounded by two sets of wedge shaped discontinuities (60~80°∠75~85° and 100~115°∠80). The average oblique length and width of the sliding source are 800 m

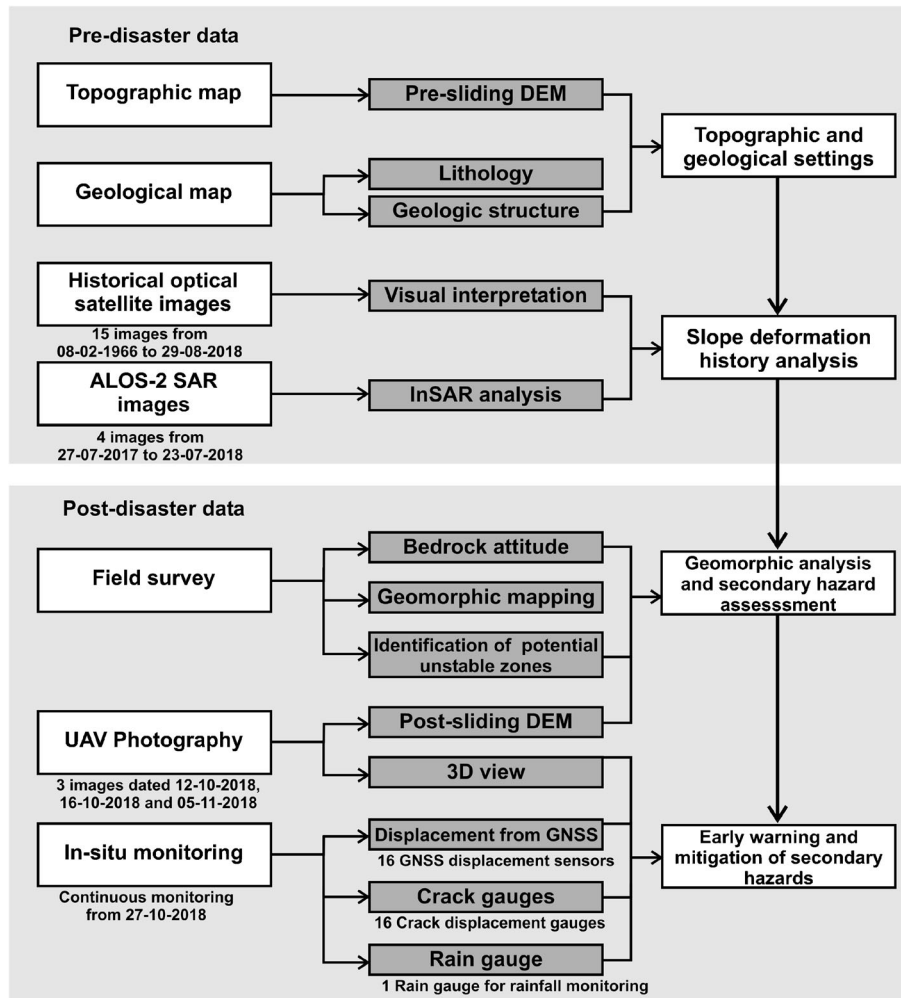


Fig. 4 Flowchart showing available data and methods used in this study

and 500 m, respectively. Observed thicknesses vary from 50 to 80 m. Consequently, total detached volume is estimated to be 20 million m^3 .

(2) Landslide transportation (II)–accumulation area (III)>

During the failure, transportation of landslide source materials (I) entrained the base rocks due to high velocity impact occurred between 2800 and 3000 m a.s.l. (II) and an additional 20 m of loose surface materials over an area of 720 m long and 170 m wide was incorporated into the falling mass, increasing the total landslide volume slightly less than 23 million m^3 . Finally, a 1-km-long (along the river valley), 85-m-high, and 500-m-wide (across the river valley) landslide dam was formed.

(3) Surge area (IV)>

Due to the strong mobility, the landslide deposits were super-elevated and reached to the opposite bank of the Jinsha River on a gentle shrubby terrain with a slope of 15° to 20°. Likewise, radial

disturbance patterns on vegetation allows tracking of the river surge induced by extremely high impulse waves generated during the landslide deposition. Firstly, flow from the resultant surge rushed towards the east riverbed, and then spread both in upstream and downstream directions. As a consequence, loose deposits and vegetal cover were extensively removed by the flow, leaving only a small amount of residual soil cover. Therefore, the boundary between finally resting landslide deposits and the area affected by water surge (IV) is clear. The former is comprised of rock mass and entrained soil. The latter is composed of dried mud. Besides run up of debris, there was a splash of water on the opposite bank. However, it was not possible to properly distinguish among the limits of the boundaries induced by the surge of landslide material and the immediate turbulence and splash of water reaching the opposite side, as we lack images immediately after the occurrence of the first event.

(4) Neighboring disturbed zones>

The detachment of 20 million m^3 of rock mass from the source area (I) severely impacted neighboring zones of the landslide, inducing long cracks and deformations due to withdrawal of

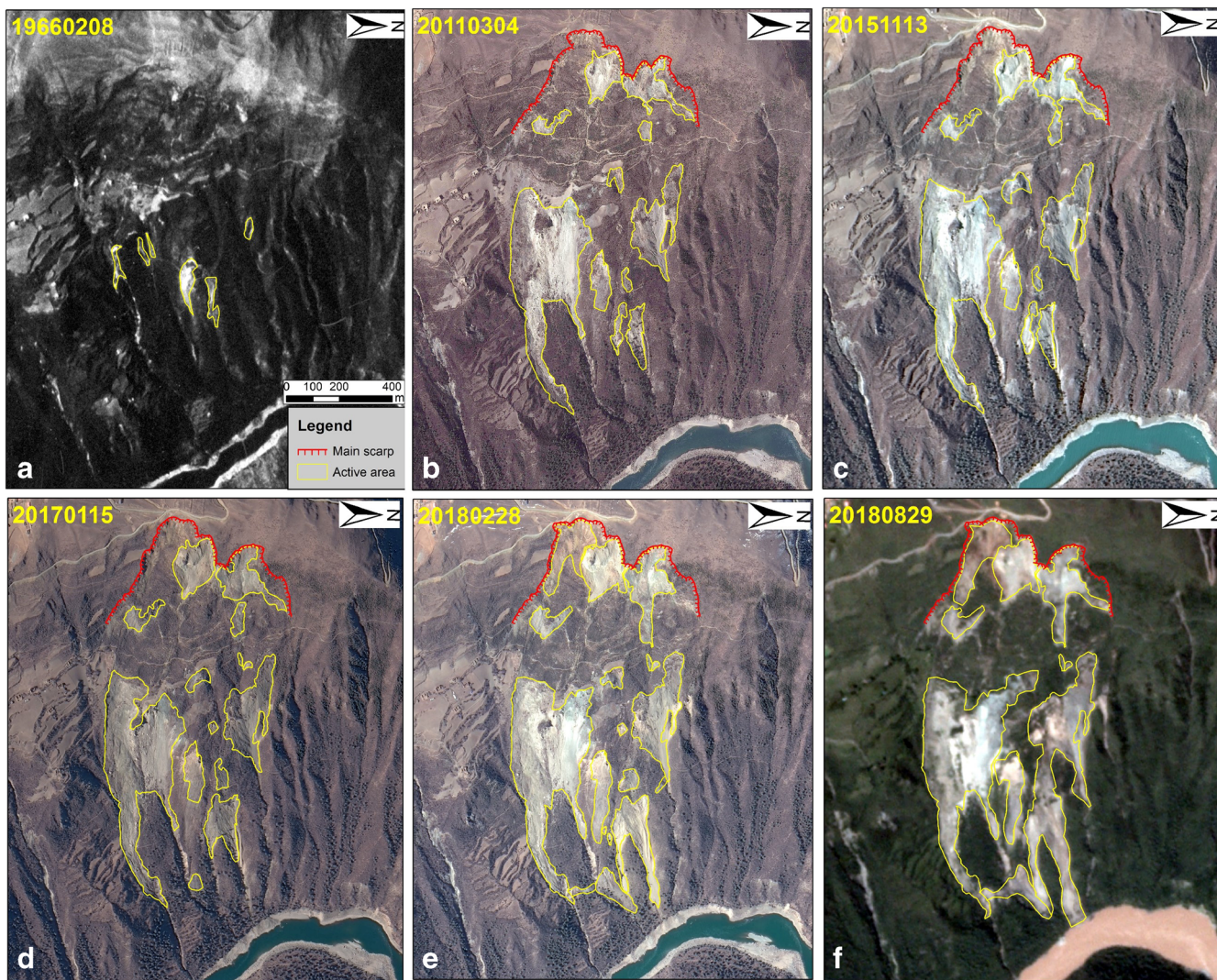


Fig. 5 Visual interpretation of historical deformation of the landslide. a KeyHole. b GeoEye-1 image. c Ziyuan ZY-3 image. d Gaofen-2 GF-2 image. e Gaofen-2 GF-2 image. f PlanetScope image. The time these images taken are shown using yyyy-mm-dd format in each figure

limit-state equilibrium. Following this, potential unstable rock masses were exposed in the surrounding area of the landslide crown further increasing the threat of consecutive landslides. These potential unstable rock masses are termed as K_1 , K_2 , and K_3 ; their locations are indicated in Fig. 8 and shown in Fig. 10.

(1) Deformed body above the headscarp (K_1)>

A series of tensile cracks with strikes of $320^\circ\sim 350^\circ$ were induced by fracturing around the source area. They are 150 m long and show a downward displacement between 30 and 50 cm (Fig. 10a). Ten to 40 cm opening of fissures is observed. Particularly, a subset extends to the right rear side of the source area with strikes between 0° and 10° . Fractures spread over an area of $3.6 \times 10^6 \text{ m}^2$ with assumed volume of $4 \times 10^6 \text{ m}^3$. Another group of cracks with a strike of 40° reached the free face, leading to a triangular unstable wedge on the left edge of the source area. This wedge became the source of the second landslide occurred on November 3.

(2) Deformed area on the south edge (K_2)>

Between 3300 and 3500 m a.s.l., rock mass with 2 to 3 m benches are found predominant (Fig. 10b). They span for 400 m, following a strike of 110° and exhibit the largest deformation at the southern edge. The overall dimensions of this compromised area are $400 \text{ m} \times 120 \text{ m}$ spanning over a 200-m elevation, leading to a total disturbed volume of roughly 1 million m^3 .

(3) Deformed area on the North edge (K_3)>

Grinded green serpentinite along with fractured and strongly weathered rocks were exposed at this edge (Fig. 10c). The top of this edge follows a fracture with a strike of 200° while its middle section shows a fracture zone with a strike of 140° . Small rock collapses are found at its base. The unstable block at this edge is a prismatic body having 550 m long, 160 m wide, and 120 m thick dimensions.

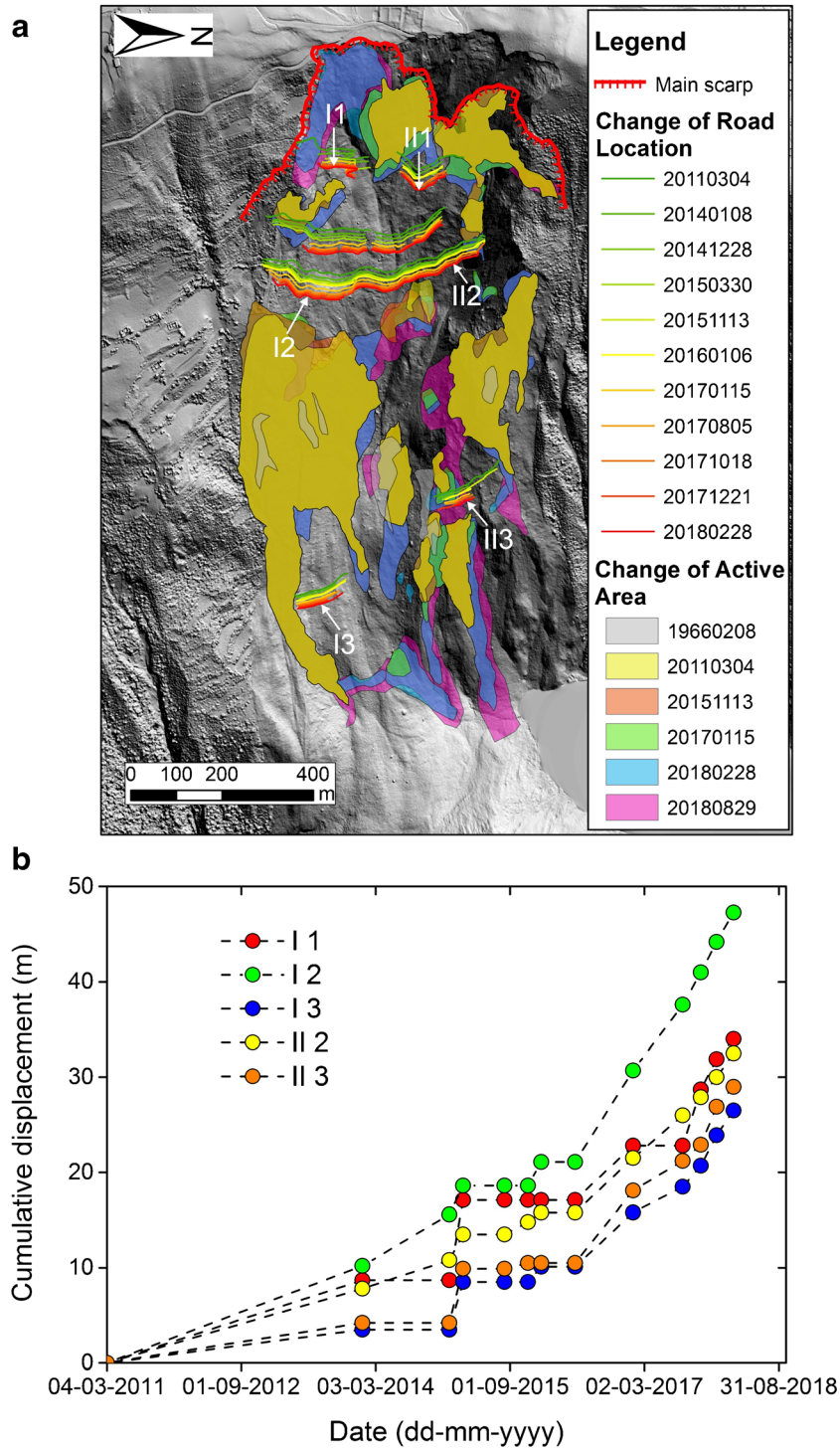


Fig. 6 a Deformation map of different zones and b their back-calculated displacement over years. Increasing displacement can be seen from the increasing size of polygons and the back-calculated displacements

Natural discharge of the first landslide lake

The water level behind the landslide dam rose quickly to 36.4 m and impounded a lake of 290 million m³. At 5 PM local time on October 12, the dam was overtopped leading to a sudden decline of the lake water level. Afterwards, on November 13, upstream and downstream courses reconnected again resulting in a discharge

channel with a bottom width of 75 m and a top width of 200 m. Water level reduced at an average rate of 1.7 m per hour, increasing up to 2 m per hour, when the discharge flow reached 10 thousands m³/s. The estimated volume of the residual dam in site after the flood discharge was 14 million m³, thus the river eroded approximately 8.3 million m³ of debris.

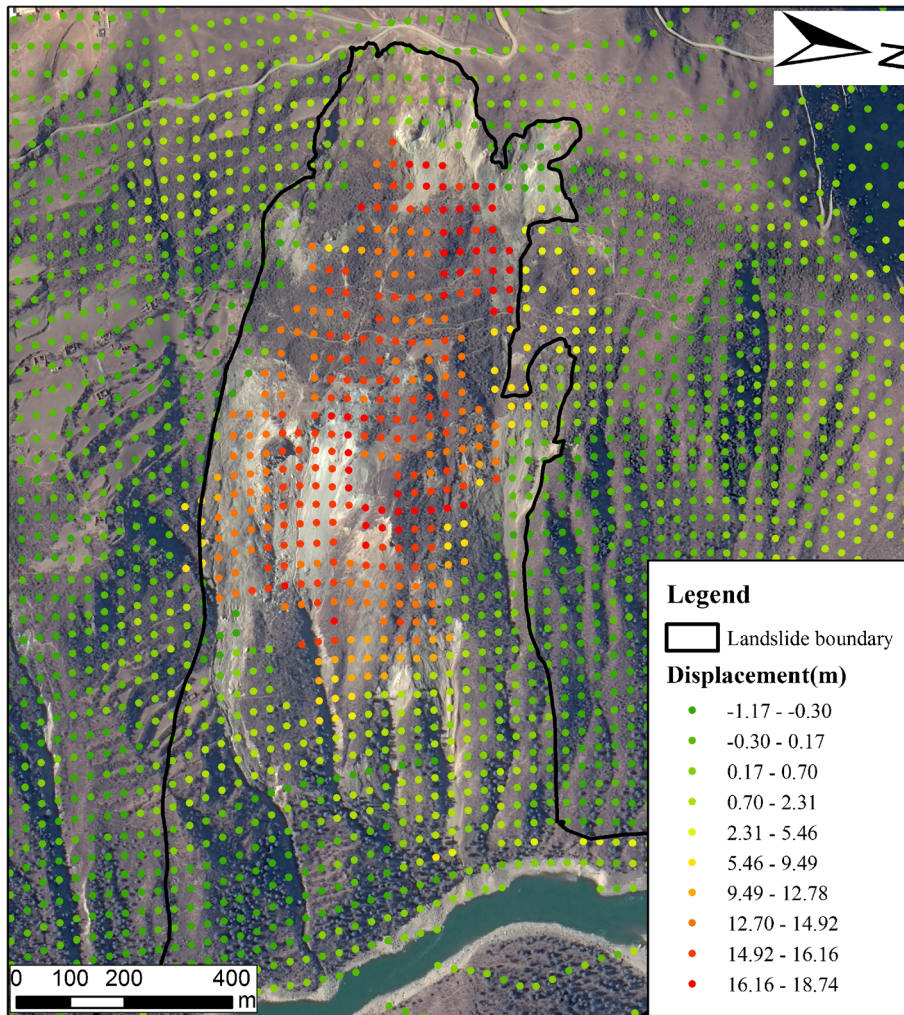


Fig. 7 Estimated landslide deformation results showing satellite line of sight (LOS) direction displacements based on pixel-offset tracking (data source provided by the Oriental Zhiyuan Technology Co., Ltd)

Characteristics of the second landslide damming river incident on November 3

On November 3, 2018, a second landslide occurred. The source of the second landslide was within the eastern edge of the crown of the October 11 event. The rock mass traveled along the slip surface formed by the first landslide, entraining a large amount of its debris. Later, the landslide was converted into a rock avalanche blocking the natural discharge channel of the Jinsha River and settled over the deposits of the first landslide. Field investigation and analysis of UAV images showed the second landslide mobilized a volume one order of magnitude lower than the first event on October 11. At the same time, deformations on neighboring zones were increased suddenly as a consequence of this subsequent landslide.

(1) Source area (A)>

The source area (A) of second landslide is located within the source of first landslide (I). The source area can be divided into two parts A1 and A2 according to the thickness and scale of the unstable rock masses

(Fig. 8b). The A1 area is located on the south side of the trailing part of the zone I, and the A2 area is located on the north side. The rock mass in zone A was exposed after the occurrence of October 11, 2018, landslide. Thus, tensile cracks on the rock masses widened gradually leading to failure. Comparison of DEMs before and after the landslide show that 60 m of previously exposed rock from the first landslide was carved within zone A, removing a volume of 3.6 million m³. Failure of A1 led to loss of additional shear resistance in A2, which in turn caused the rock mass to collapse and further removal of more than 1 million m³ of rock mass had occurred. The main scrap has a green-white color, indicating presence of chlorite. Rock mass above the headscarp is still unstable; thus, rock falls continue to occur as a result of large cracks and fractures. However, large-scale collapses are unlikely as the whole structure is supported on structurally competent hard gneiss.

(2) Transportation and entrainment area (B)>

Detached rock masses from the source traveled along the slip surface formed by the October 11, 2018, landslide,

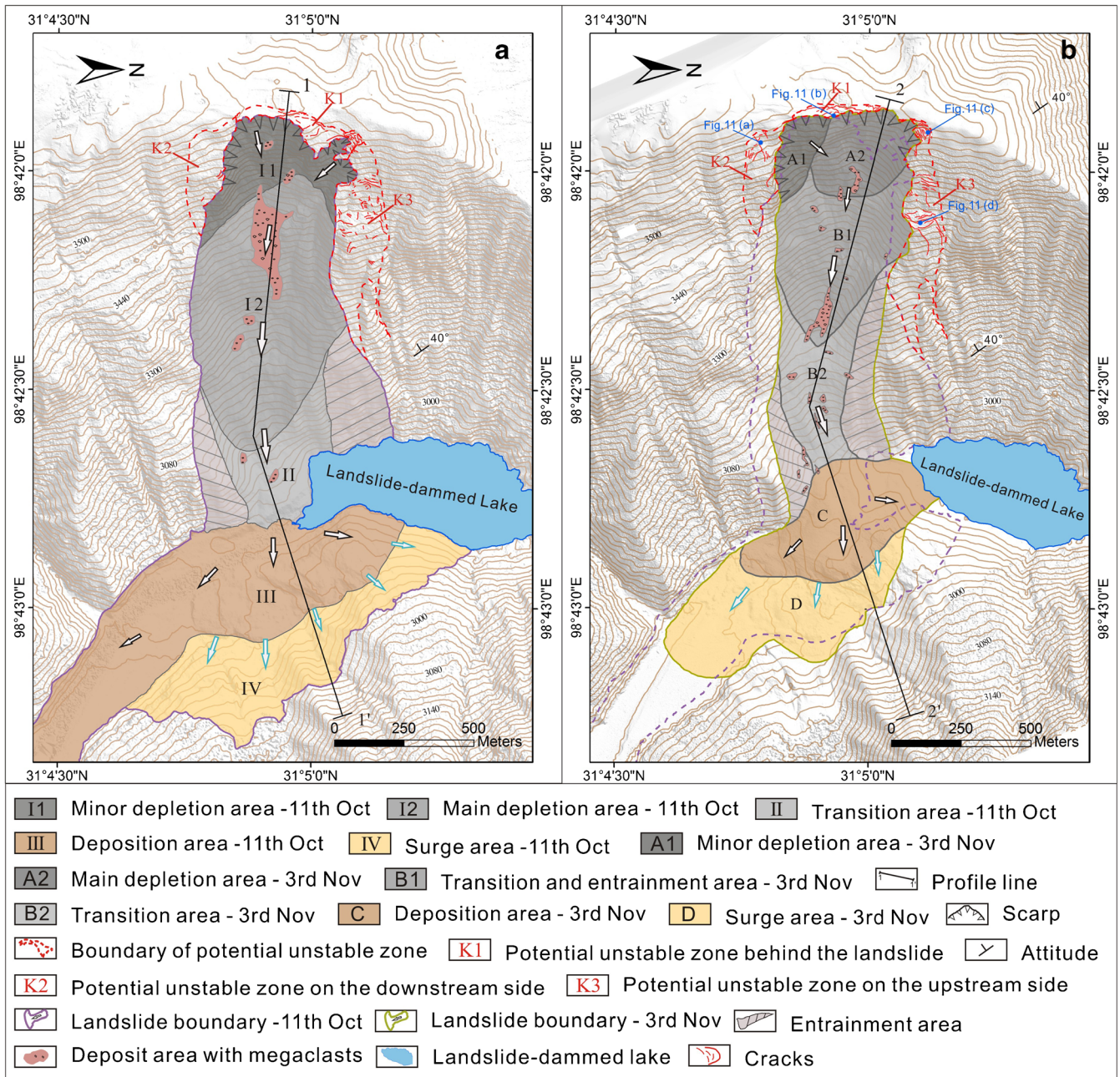


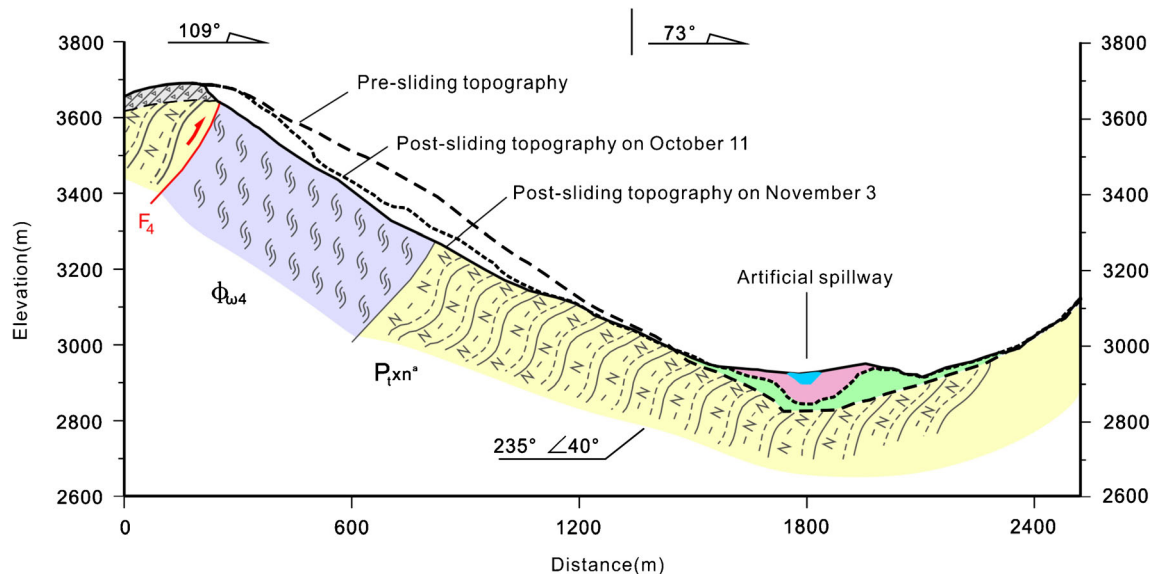
Fig. 8 Geomorphic maps for both the events. **a** First landslide event on October 11, 2018. **b** Second landslide event on November 3, 2018

entraining materials already left by the first landslide. The previously conformed slip surface and transportation zone was significantly eroded making a concave slope of 15° on an average.

During sliding over moderately hard gneiss between 2900 and 3100 m a.s.l., since the slope was steeper, the entrainment was not strong to incorporate significant amounts of material. Therefore, changes on the surface were not severe. Total mobilized volume was less than 8.5 million m³, and most of them are deposited over debris laid down by the October 11 landslide.

(3) Deposition area (C)>

Landslide material from the November 3 event rushed to settle over the natural discharge channel of the Jinsha River, damming it again. Total volume of the landslide deposits reached 9.3 million m³ increasing the height of the dam by 50 m, making it 135 m at the maximal. Thus, a 31 million m³ landslide dam was generated as the consequence of combined actions of both landslides.



Legend

P_{1xn}^*	Upper Proterozoic Xionsong Group Gneiss Formation		Artificial spillway
Φ_{w4}	Variscan jinshajiang ultramafic belt and serpentinite		Amphibole plagioclase gneiss
F_4	Fault		Serpentinite
	Landslide deposits on November 3		Quaternary overburden
	Landslide deposits on October 11		

Fig. 9 Longitudinal profile of the landslides showing both the events. The profile lines are taken along 1–1' and 2–2' from the geomorphic map

(4) Landslide-affected surrounding areas

After the second landslide, the large scarp of the October 11 landslide became even more exposed and wider cracks are observed as shown in Fig. 11. Contrarily, areas immediately below the source of November 3 failure looked overall stable. Small rock collapses were observed in the aftermath of the previous landslides (October 11 and November 3), but no pervasive large deformations or instabilities are expected. Extensive cracking (with 17° strike and 20 to 50 cm thick) are observed at the base of the first landslide at heights between 3500 and 3600 m a.s.l. Serpentinite at this location is green and white colored, highly fractured, with high content of chlorite and can be broken even by hand (Fig. 11).

Emergency rescue operation, monitoring, and early warning system

Sudden large-scale landslide disasters require immediate response actions in order to prevent anticipated secondary hazards. Immediately after the first landslide on October 11, 2018, we mapped and characterized potential failure zones as discussed in the “Characteristics of first slope collapse” section. Different monitoring stations were installed on site and connected to a real-time early warning system hosted by our institute (Huang et al. 2013, 2015). Through the early warning system, two secondary landslide failures that occurred on November 3 and November 6 were predicted

successfully. This section details the success story of the emergency response, early warning, and mitigation of secondary landslide disasters.

Monitoring station deployment

After the October 11, 2018, event, we installed 16 GNSS receivers, 16 crack gauges, and 1 rainfall gauge over the pre-found potential failure zones (see the “Characteristics of first slope collapse” and “Characteristics of the second landslide damming river incident on November 3” sections). A part of deployed equipment was damaged when the second landslide occurred. The layout of the installed monitoring equipment is shown in Fig. 12.

Event response of monitoring data

GNSS satellite displacement monitoring points were placed surrounding the headscarp of the October 11 landslide. Until November 3, a steady, almost linear-trending displacement had been observed, until a sudden initial increase was noticed just before the second landslide. After the initial increase, displacement accelerated compared to what had been observed earlier in October (Fig. 13a).

Largest displacements were recorded by probes GP 1, 2, and 6. First two were on the right rear edge (left if we look towards direction of motion) of the second landslide source area, while

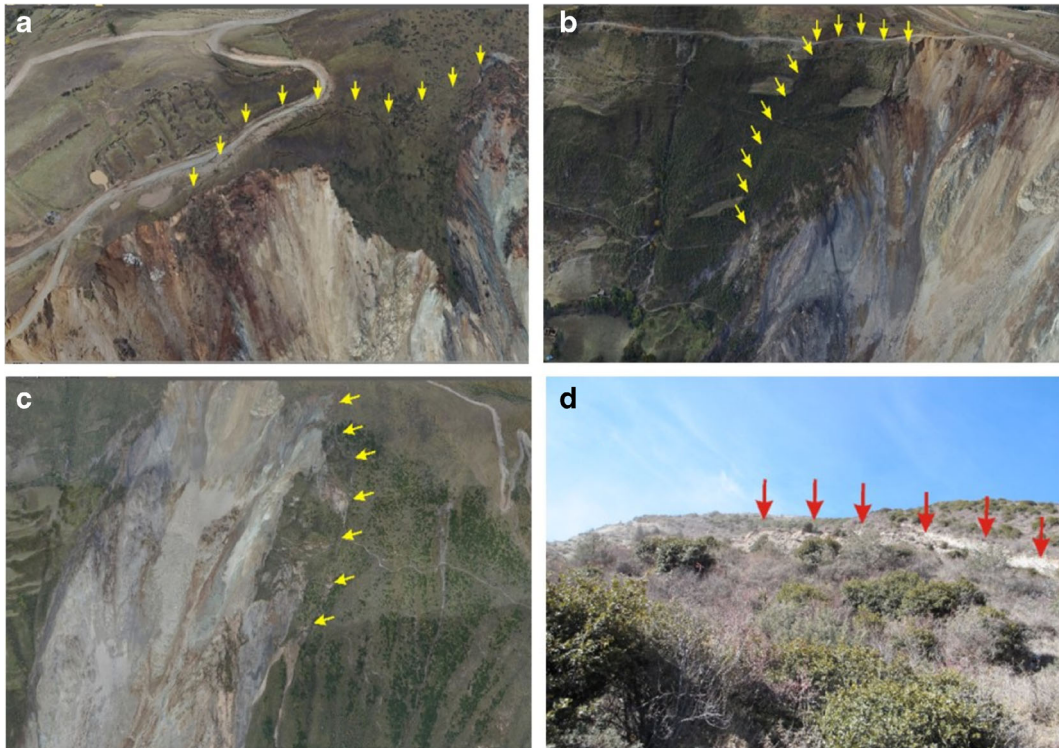


Fig. 10 a Crack distribution in K1 area above the headscarp (the arrow in the figure refers to the crack zone). b Crack distribution in K2 area on the true right side (the arrow in the figure refers to the crack zone). c Panorama of lateral shear fractures in upper reaches of K3 area on the true left side. d Shear crack on the upstream side of the K3 zone (the arrow in the figure refers to the crack zone)

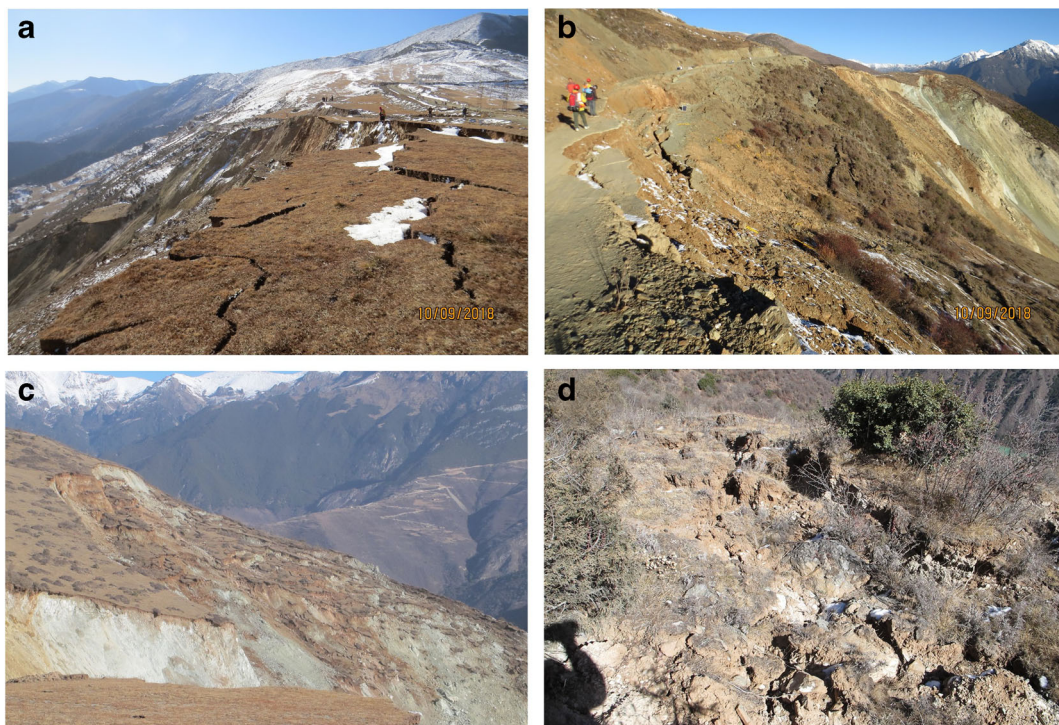


Fig. 11 Location of tension cracks and potential failure paths after the first event. a Tension cracks in the trailing part of K1 area. b Platform of slope dislocation in K2. c Fracture zone of serpentinite in the upper part of K3. d Intense tensile fractures in the middle of K3. Locations of K1, K2, and K3 are shown in Fig. 8b

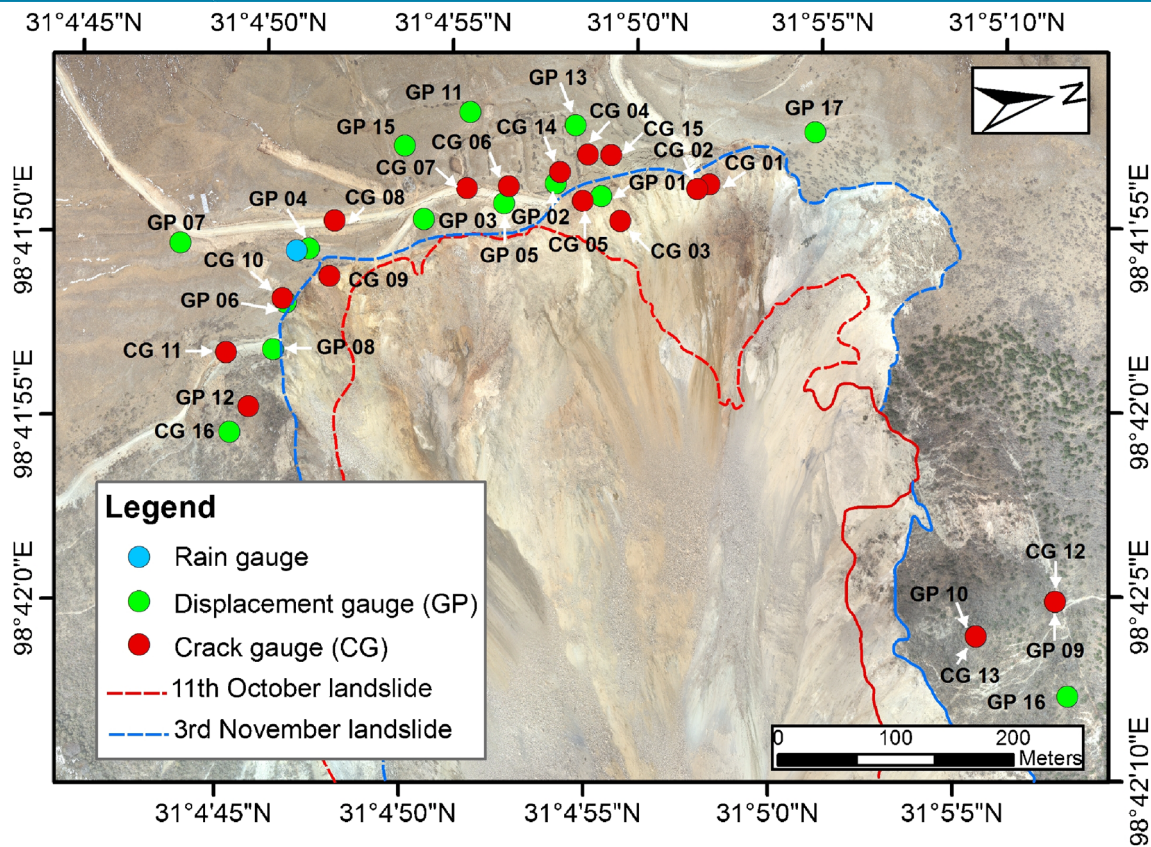


Fig. 12 Location map of installed monitoring instruments. GP refers to the GNSS displacement sensors and CG refers to crack gauges

other six were on a steep ridge in K2 that is strongly affected by the small collapses of unstable rocks. Displacement trends at other stations (GP 3, 4, 5, and 7) were lower as they were located further away from the sliding surface.

The crack gauges were placed on tensile cracks behind the source area (I) of October 11 landslide. Measured time histories are presented in Fig. 13b. Gauges CGo1, CGo2, CGo3, and CGo5 broke before the November 3 event. CGo4 is located 20 m behind the A1 area and spans along a crack oriented in the north-south direction. Sudden increases were observed three times, and they are consistent with the increase in recorded displacement time histories. First increase occurred at 18:00 local time on November 3, 2018, during the slope failure. The other two were observed at 8:00 on November 11 and at 11:00 on November 21. On both occasions small rockfalls were observed around the exposed scarp. Agreement between GNSS logs and crack gauge monitoring show how they reflect the deformation process of the whole slope, making GNSS data and CG data particularly well suited for compiling landslide early warning models.

Monitoring system and early warning model

In general, threshold breaching models are considered to calibrate landslide early warning systems (Intrieri et al. 2012; Manconi and Giordan 2015). However, this approach is not well suited for cases where slope failure has already occurred. Therefore, another procedure had to be sought for responding the particular needs arising during an emergency. An alternate option was proposed

by Xu et al. (2009a) considering changes on the deformation rate obtained from the field measurements, compared to baseline estimates of secondary constant creep rates, through the improved tangential angle (α) criterion.

The method can be described briefly as follows: at first, estimates of the steady-state creep rate (ν_o) are calculated by computing the average of a large number of stable measurements. Once a reliable baseline has been obtained, displacement rates ν (ratio of displacement change with unitary measurement time) are computed and compared with this threshold through the following expression

$$\alpha = \text{atan}\left(\frac{\nu}{\nu_o}\right) \quad (1)$$

Values of ν and α are compared to predefined thresholds to issue warnings, following guidelines presented in Fig. 14. For further details on the method, the reader is referred to Xu et al. (2011).

The early warning system performed remarkably well as predictor of the slope failure on November 3. Assessment of recorded displacement collected since October 26 allowed for a definition of a clear baseline for ν_o , issuing a clear imminent landslide early warning 24 h before the disaster. Data from crack gauge CGo4 is shown in Fig. 15a. Likewise, on November 6, a milder warning was issued (vigilance level), as a sudden deformation buildup was observed (Fig. 15b) and a minor landslide occurred. However, the deformation was not sustained in time.

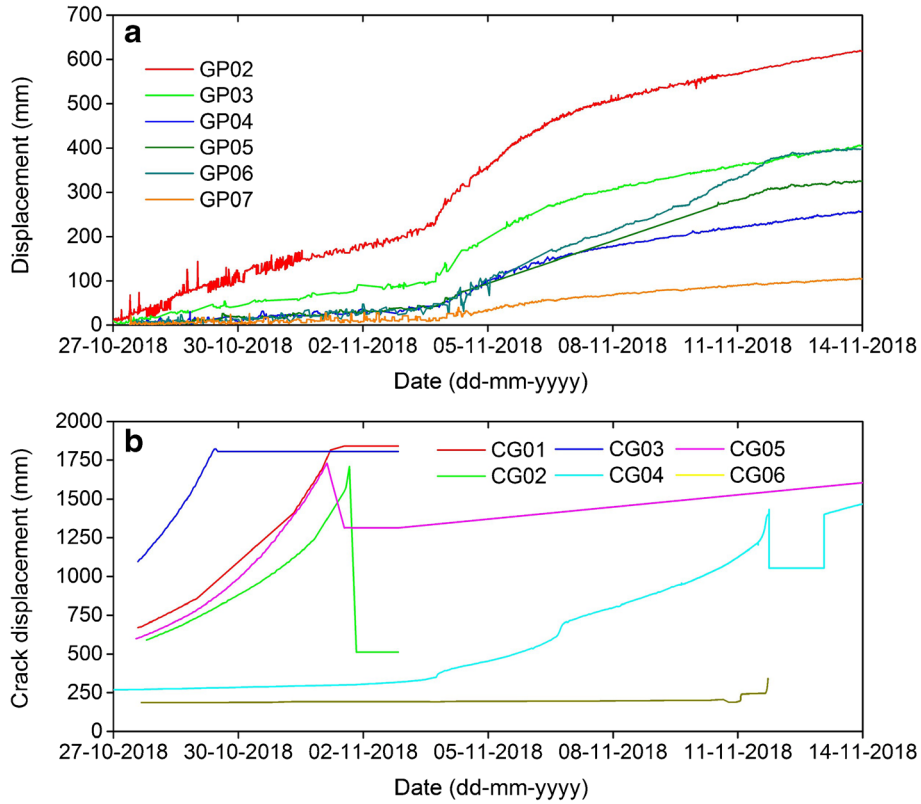


Fig. 13 Continuous monitoring of displacement through a GNSS and b crack gauges from October 27, 2018

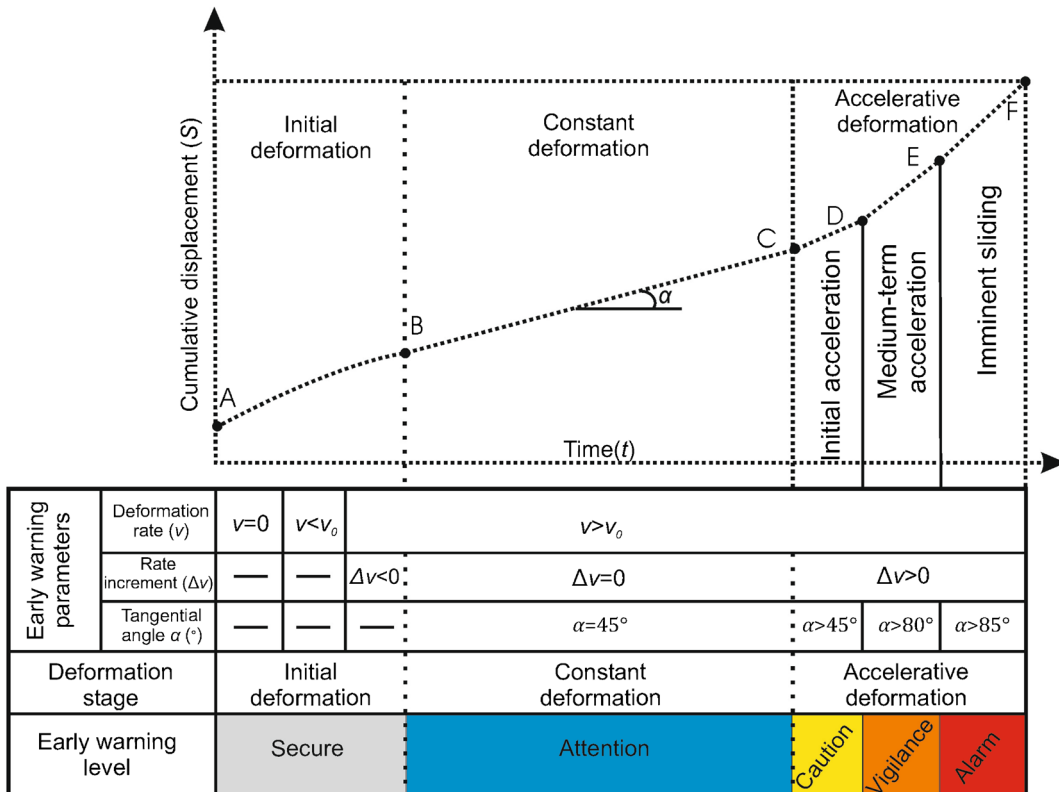


Fig. 14 Outline of the early warning model

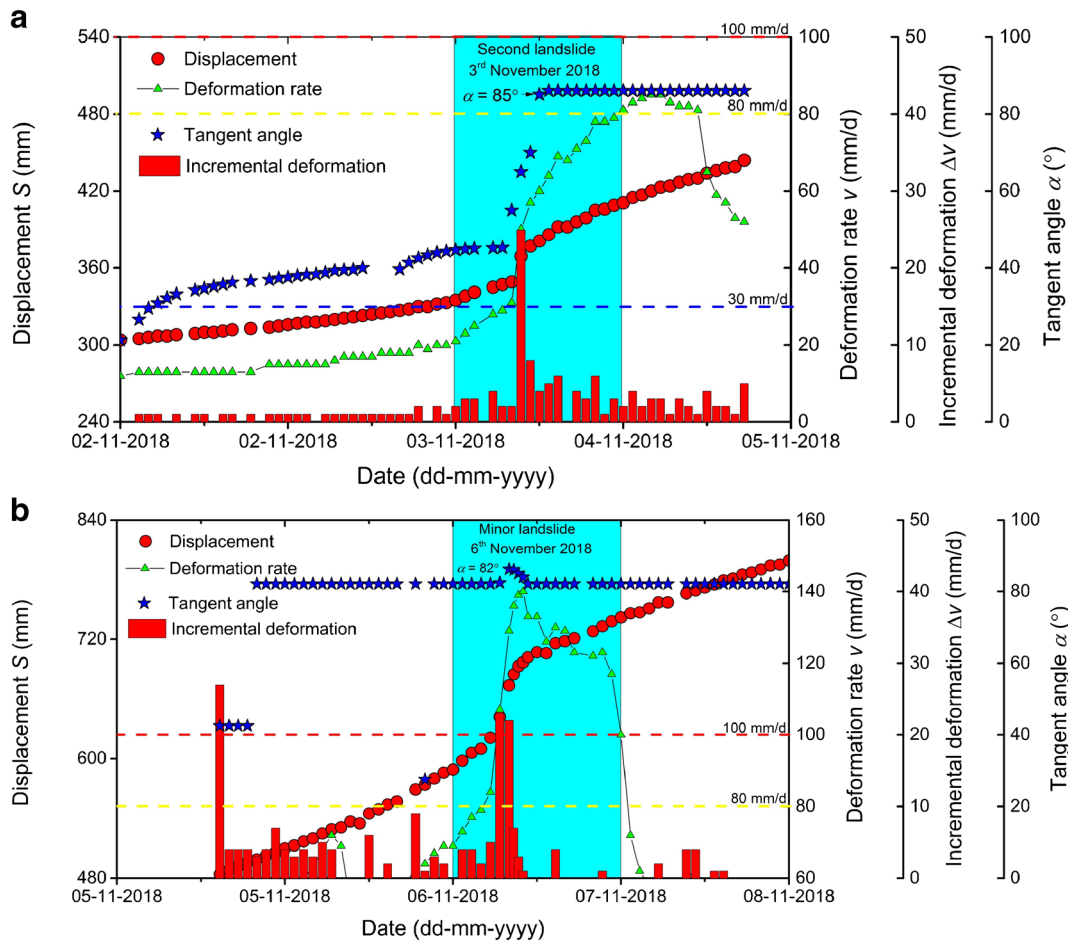


Fig. 15 Early warning charts using displacements and crack gauges. **a** Second landslide event on November 3, 2018. **b** Third landslide event on November 6, 2018 (using crack gauge CG04)

As a result, the monitoring system performed remarkably well in predicting the landslide on November 3, 24 h before it happened, while it supported construction of artificial spillway ensuring safety during emergency response. It is prudent to point out that reliable control of the emergency response actions was achieved with the help from early warning of secondary hazards using dense numbers of measuring points deployed at diverse locations.

Discussion

The Baige slope failures and subsequent events present interesting and relevant outcomes to advance the current state of the art regarding mitigation of landslides risks worldwide. Firstly, the trigger of the first event on October 11 remains elusive. Taking into account the state of borderline limit equilibrium, a complex and nonlinear interaction of ambient factors could have led to failure. Upcoming tests with the aim of assessing the rheological behavior of both gneiss and serpentinite to be carried in the SKLGP will allow for more insights to this.

The question if there are other critically stable slopes along the canyon of the Jinsha River is also a concern. Albeit earthquake shaking was not relevant in this case, it may play a role in the future, particularly leading to correlated failure of several, even

hundreds slopes if a large rupture would occur along the Jinsha River Fault zone. Furthermore, in steep mountainous terrains, gravitational sliding of slopes are prominent being in a state of limit-equilibrium, and therefore, even low magnitude earthquakes ($M_w \sim 5.0$) could lead to landsliding. There is evidence of extensive cracking and disruption of slopes due to low magnitude earthquakes (Alfaro et al. 2012; Nappi et al. 2018).

Thus, there is a pressing need for systematic early warning of the whole canyon of the Jinsha River. The system should be able to take images at a regular rate, ideally weekly, and should be able to deploy in the aftermath of earthquakes with magnitude larger than M_w 4.5.

Other issue to address is the stability of landslide dams. Two widely recognized empirical equations for quick assessment of dam stability show that both landslide dams (October 11 and November 3) are not long-term stable. The first criteria is the dimensionless blockage index (DBI) (Eq. 2) proposed by Ermini and Casagli (2003). It is indicative of instability if its value exceeds 3.08.

$$DBI = \text{Log} \left(\frac{A_b H_d}{V_d} \right) \quad (2)$$

Table 2 Matrix for a quick qualitative assessment of the individual landslide dams proposed after the 2008 Wenchuan earthquake (Xu et al. 2009b)

Catastrophic landslide breach possibility	Criteria Dam height (m)	Barrier lake capacity (million m ³)	Characteristics of landslide dam body composition
Very high	> 100	> 10	> 50% of soil and rock fragments and grain sizes from 20 to 200 mm. Other 50% are both larger and finer.
High	50–100	1–10	Soil and fragments of rock with few boulders and blocks; > 50% of soil and rock fragments; 20 to 200 mm grain size. Boulders and blocks; grain size > 200 mm.
Moderate	25–50	0.1–1	Boulders and blocks with little soil and rock fragments; > 50% of boulders and blocks; grain size > 200 mm.
Low	≤ 25	≤ 0.1	Boulders and blocks; grain size > 200 mm.

where V_d is the landslide dam volume in m³, H_d is its height in meters, and A_b is the catchment area of the Jinsha River at the landslide dam location in km². A_b is measured as 17,000 km². For the first landslide dam, $V_d = 20.4$ million m³ and $H_d = 85$ m, leading to a DBI of = 4.85. For the second landslide dam, $V_d = 31$ million m³, $H_d = 135$ m, thus DBI = 4.87.

Dong et al. (2011) have proposed a model that takes into account dam dimensions, while providing for an actual estimate of the probability of breaching (Eq. 3).

$$L_s = -2.2\text{Log}(A_b) - 3.76\text{Log}(H_d) + 3.17\text{Log}(W_d) + 2.85\text{Log}(L_d) + 5.93 \quad (3)$$

$$P_f = \frac{e^{-L_s}}{1 + e^{-L_s}}$$

where W_d , L_d , and P_f are the dam width along the river direction, the dam length across river flow, and the probability of failure, respectively. For both the first and second landslide dams, a probability of failure larger than 99% is estimated. It must be remarked that these equations were developed for single-event barrier dams. Therefore, they could not properly model successive

damming, where consolidation by impact is critical. This could explain why the second dam did not breach after almost a week being 50 m higher, while the first one did just after a single day.

The DBI and Dong et al. (2011) probability of failure estimates are just a sample of a wide set of geomorphic indices which are often used to quantitatively assess landslide dam stability (Korup 2004; Cui et al. 2009; Dal Sasso et al. 2014; Tacconi Stefanelli et al. 2016). These empirical indices employ easily and quickly collectable morphometric parameters related to the landslide, the dam, the river, the valley, and the lake, involving simple relationships while posing no consideration to the internal structure and composition of the landslide dam materials. These shortcomings make them highly unreliable during emergency scenarios. For example, if criteria considered in this study are inverted to find the critical catchment areas leading to threshold values of DBI = 3.08 and $P_f = 0.5$, values differing a whole order of magnitude are found. It must be considered that decision makers have to follow a course of action quickly during the emergency. Further adjustment of simplified equations is extremely challenging considering the complex and often unknown dam breach process and geological parameters.

On the other hand, Xu et al. (2009bb) proposed guidelines for assessment of landslide dam catastrophic failure based on experience obtained in the aftermath of the 2008 Wenchuan Earthquake (Table 2). Besides involving dam geometry parameters, they consider general information on the dam body properties, allowing for application of these guidelines after a brief inspection. Clearly, both landslide dams (October 11 and November 3) were at high risk of catastrophic breaching as their heights were larger than 50 m and most relevant; their impounded lakes were more than an order of magnitude than the threshold of 10 million m³.

If continuous and steady monitoring of valleys is available, it is possible to identify critically creeping slopes in advance. Then, numerical models can be adopted for quick and physically reliable estimations of stability instead of empirical indices. Further, Bayesian analysis (Lee 2012) can also be employed to select models that represent better what is observed during the emergency.

Conclusions

Two consecutive landslides dammed lakes in the Jinsha River, encompassing an impoundment volume of 290 and 524 million m³, at the border between Sichuan province and Tibet, were formed by successive landslides occurred on October 11 and November 3. Mass wasting and mobilization of a total volume of 36 million m³ took place. While the first lake started draining naturally just a day after the landslide, the second one kept increasing its volume during the next 5 days, warranting remedial actions by local authorities. Potential consequences of the landslide dam breach led local authorities to proceed with construction of a spillway. The construction of the spill way was supported by a landslide early warning system developed by the authors' institute, State Key Laboratory of Geohazard Prevention and Geoenvironment Protection (SKLGP). The system successfully predicted the occurrence of the second landslide and a minor rock fall, while avoiding disruption of excavation tasks by false alarms. Albeit loss of life was completely averted, moderate flooding was induced by quick discharge through the man-made spillway.

We collected high-resolution satellite images and InSAR data to estimate displacement traces on the slope prior collapse. We found

that the landslide had experienced creep displacement in the past decades. Particularly, more than 40 m were observed in the past decade and we measured 25 more in the year prior to the emergency. Thus, the slope was in an unstable equilibrium making it failure imminent. It must be pointed out that this information was available before the emergency. Therefore, it was possible to have done more mitigation procedures if continuous monitoring of the Jinsha River Canyon between Sichuan Province and Tibet had been available. This could have reduced direct losses further. Particularly forecasting modeling of the slope failure, damming process and prospective flooding could have been done in advance, instead of relying in empirical models for quickly assessing landslide dam stability, which have variations of at least one order of magnitude. This representative case shows the advantages of performing continuous monitoring and early warning of potential landslide sites by integrating remote sensing and in situ landslide monitoring methods can significantly reduce landslide risk.

Acknowledgments

We want to thank the contribution of Jie Liu, Cheng Zhao, Zetao Feng, Fan Yang, Lanxin Dai, and Xiangyang Dou for supporting in data collection and field investigation.

Funding This research is financially supported by the National Science Fund for Outstanding Young Scholars of China (Grant No. 41622206), the Funds for Creative Research Groups of China (Grant No. 41521002), the Fund for International Cooperation (NSFC-RCUK_NERC), Resilience to Earthquake-induced landslide risk in China (Grant No. 41661134010), and the fund for Team Project of Independent Research of SKLGP (Grant Nos. SKLGP2016Z001 and SKLGP2016Z002).

References

- Alfaro P, Delgado J, Garcia Tortosa F, Lenti L, Lopez J, Lopez-Casado C, Martino C (2012) Widespread landslides induced by the Mw 5.1 earthquake of 11 May in Lorca, SE Spain. *Eng Geol* 137:138–40–52
- Ambraseys N, Douglas J (2004) Magnitude calibration of north Indian earthquakes. *Geophys J Int* 159:165–206
- Cascini L, Fornaro G, Peduto D (2009) Analysis at medium scale of low-resolution DInSAR data in slow-moving landslide-affected areas. *ISPRS J Photogramm Remote Sens* 64:598–611. <https://doi.org/10.1016/j.isprsjprs.2009.05.003>
- Chai H, Liu H, Zhang Z (2000) The temporal-spatial distribution of damming landslides in China. *J Mt Sci* 18(Suppl):51–54
- Cui P, Zhu Y, Han Y et al (2009) The 12 May Wenchuan earthquake-induced landslide lakes: distribution and preliminary risk evaluation. *Landslides* 6:209–223. <https://doi.org/10.1007/s10346-009-0160-9>
- Dal Sasso SF, Sole A, Pascale S et al (2014) Assessment methodology for the prediction of landslide dam hazard. *Nat Hazards Earth Syst Sci* 14:557–567. <https://doi.org/10.5194/nhess-14-557-2014>
- Dong J, Tung Y, Chen C, Liao J, Pan Y (2011) Logistic regression model for predicting the failure probability of landslide dam. *Eng Geol* 117(1–2):52–61
- Ermini I, Casagli N (2003) Prediction of behaviour of landslide dams using a geomorphological dimensionless index. *Earth Surf Process Landf* 28(1):31–47
- Fan X, Tang CX, van Westen CJ, Alkema D (2012a) Simulating dam-breach flood scenarios of the Tangjiashan landslide dam induced by the Wenchuan Earthquake. *Nat Hazards Earth Syst Sci* 12:3031–3044. <https://doi.org/10.5194/nhess-12-3031-2012>
- Fan X, van Westen CJ, Korup O et al (2012b) Transient water and sediment storage of the decaying landslide dams induced by the 2008 Wenchuan earthquake, China. *Geomorphology* 171–172:58–68. <https://doi.org/10.1016/j.geomorph.2012.05.003>
- Fan X, van Westen CJ, Xu Q et al (2012c) Analysis of landslide dams induced by the 2008 Wenchuan earthquake. *J Asian Earth Sci* 57:25–37. <https://doi.org/10.1016/j.jseas.2012.06.002>
- Fan X, Xu Q, Scaringi G et al (2017) Failure mechanism and kinematics of the deadly June 24th 2017 Xinmo landslide, Maoxian, Sichuan, China. *Landslides* 14:2129–2146. <https://doi.org/10.1007/s10346-017-0907-7>
- Fan X, Zhan W, Dong X et al (2018a) Analyzing successive landslide dam formation by different triggering mechanisms: the case of the Tangjiawan landslide, Sichuan, China. *Eng Geol* 243:128–144. <https://doi.org/10.1016/j.enggeo.2018.06.016>
- Fan X, Xu Q, Scaringi G (2018b) Brief communication: post-seismic landslides, the tough lesson of a catastrophe. *Nat Hazards Earth Syst Sci* 18:397–403. <https://doi.org/10.5194/nhess-18-397-2018>
- Farina P, Colombo D, Fumagalli A et al (2006) Permanent Scatterers for landslide investigations: outcomes from the ESA-SLAM project. *Eng Geol* 88:200–217. <https://doi.org/10.1016/j.enggeo.2006.09.007>
- Guzzetti F, Manunta M, Ardizzone F et al (2009) Analysis of ground deformation detected using the SBAS-DInSAR technique in Umbria, Central Italy. *Pure Appl Geophys* 166:1425–1459. <https://doi.org/10.1007/s00024-009-0491-4>
- Huang R (2012) Mechanisms of large-scale landslides in China. *Bull Eng Geol Environ* 71:161–170. <https://doi.org/10.1007/s10064-011-0403-6>
- Huang R, Huang J, Ju N et al (2013) WebGIS-based information management system for landslides triggered by Wenchuan earthquake. *Nat Hazards* 65:1507–1517. <https://doi.org/10.1007/s11069-012-0424-x>
- Huang J, Huang R, Ju N et al (2015) 3D WebGIS-based platform for debris flow early warning: a case study. *Eng Geol* 197:57–66. <https://doi.org/10.1016/j.enggeo.2015.08.013>
- Intrieri E, Gigli G, Mugnai F et al (2012) Design and implementation of a landslide early warning system. *Eng Geol* 147–148:124–136. <https://doi.org/10.1016/j.enggeo.2012.07.017>
- Korup O (2004) Geomorphometric characteristics of New Zealand landslide dams. *Eng Geol* 73:13–35. <https://doi.org/10.1016/j.enggeo.2003.11.003>
- Lee P (2012) Bayesian statistics, an introduction, 4th edn. Wiley, Hoboken
- Liu C, Li W, Wu H et al (2013) Susceptibility evaluation and mapping of China's landslides based on multi-source data. *Nat Hazards* 69:1477–1495. <https://doi.org/10.1007/s11069-013-0759-y>
- Manconi A, Giordano D (2015) Landslide early warning based on failure forecast models: the example of the Mt. de La Saxe rockslide, northern Italy. *Nat Hazards Earth Syst Sci* 15:1639–1644. <https://doi.org/10.5194/nhess-15-1639-2015>
- Monserrat O, Crosetto M, Luzi G (2014) A review of ground-based SAR interferometry for deformation measurement. *ISPRS J Photogramm Remote Sens* 93:40–48. <https://doi.org/10.1016/j.isprsjprs.2014.04.001>
- Nappi R, Alessio G, Gaudiosi G, Nave R, Marotta E, Siniscalchi V, Civico R, Plizzimenti L, Peluso R, Belviso P, Porfido S (2018) The 21 August $M_d = 4.0$ Casamicciola earthquake: first evidence of coseismic normal surface faulting at the Ischia Volcanic Island. *Seismol Res Lett* 89(4):1323–1334
- Peteley D (2018) A dangerous valley—blocking landslide in Jomda County Tibet. American Geophysical Union, Landslides Blog. <https://blogs.agu.org/landslideblog/2018/11/12/jomda-county-landslide-2/>. November 12th, 2018
- Peterman V (2015) Landslide activity monitoring with the help of unmanned aerial vehicle. *ISPRS - Int Arch Photogramm Remote Sens Spat Inf Sci XL-1/W4:215–218*. <https://doi.org/10.5194/isprarchives-XL-1-W4-215-2015>
- Ren Z, Zhang Z, Yin J (2017) Erosion associated with seismically-induced landslides in the middle Longmen Shan region, eastern Tibetan plateau, China. *Remote Sens* 9:864. <https://doi.org/10.3390/rs9080864>
- Schlögel R, Doubre C, Malet J-P, Masson F (2015) Landslide deformation monitoring with ALOS/PALSAR imagery: a D-InSAR geomorphological interpretation method. *Geomorphology* 231:314–330. <https://doi.org/10.1016/j.geomorph.2014.11.031>
- Sijing W, Guohe L, Qiang Z, Chaoli L (2010) Engineering geological study of the active tectonic region for hydropower development on the Jinsha River, upstream of the Yangtze River. *Acta Geol Sin English Ed* 74:353–361. <https://doi.org/10.1111/j.1755-6724.2000.tb00474.x>
- Storchak D, Di Giacomo D, Bondar I, Engdahl E, Harris J, Lee W, Villasenor A, Bormann P (2013) Public release of the ISC-GEM global instrumental earthquake catalogue (1900–2009). *Seismol Res Lett* 84(5):810–815
- Stumpf A, Malet J-P, Delacourt C (2017) Correlation of satellite image time-series for the detection and monitoring of slow-moving landslides. *Remote Sens Environ* 189:40–55. <https://doi.org/10.1016/j.rse.2016.11.007>
- Tacconi Stefanelli C, Segoni S, Casagli N, Catani F (2016) Geomorphic indexing of landslide dams evolution. *Eng Geol* 208:1–10. <https://doi.org/10.1016/j.enggeo.2016.04.024>
- Tian B, Li Z, Zhang M et al (2017) Mapping thermokarst lakes on the Qinghai–Tibet plateau using nonlocal active contours in Chinese GaoFen-2 multispectral imagery.

- IEEE J Select Top Appl Earth Observ Remote Sens 10:1687–1700. <https://doi.org/10.1109/JSTARS.2017.2666787>
- Türk T (2018) Determination of mass movements in slow-motion landslides by the Cosi-Corr method. *Geomat Nat Haz Risk* 9:325–336. <https://doi.org/10.1080/19475705.2018.1435564>
- Turner D, Lucieer A, de Jong S (2015) Time series analysis of landslide dynamics using an unmanned aerial vehicle (UAV). *Remote Sens* 7:1736–1757. <https://doi.org/10.3390/rs70201736>
- US Geological Survey (2018) Earthquake Catalog. <https://earthquake.usgs.gov/earthquakes/>. Accessed 24 Dec 2018
- Wang SJ, Li GH, Zhang Q, Lan CL (2000) Engineering geological study of the active tectonic region for hydropower development on the Jinsha River, upstream of the Yangtze River. *Acta Geol Sin Ed* 74:353–361
- Wells DL, Coppersmith KJ (1994) New empirical relationships among magnitude, rupture length, rupture width, rupture area, and surface displacement. *Bull Seismol Soc Am* 84(4):974–1002
- Wu LZ, Zhou Y, Sun P, Shi JS, Liu GG, Bai LY (2017) Laboratory characterization of rainfall-induced loess slope failure. *Catena* 150:1–8
- Xu Q, Zeng Y, Qian J et al (2009a) Study on a improved tangential angle and the corresponding landslide pre-warning criteria. *Geol Bull China* 28(4):501–505
- Xu Q, Fan X-M, Huang R-Q, Westen CV (2009b) Landslide dams triggered by the Wenchuan Earthquake, Sichuan Province, south west China. *Bull Eng Geol Environ* 68:373–386. <https://doi.org/10.1007/s10064-009-0214-1>
- Xu Q, Yuan Y, Zeng Y, Hack R (2011) Some new pre-warning criteria for creep slope failure. *SCIENCE CHINA Technol Sci* 54:210–220. <https://doi.org/10.1007/s11431-011-4640-5>
- Zhang D, Wang G, Yang T et al (2013) Satellite remote sensing-based detection of the deformation of a reservoir bank slope in Laxiwa Hydropower Station, China. *Landslides* 10:231–238. <https://doi.org/10.1007/s10346-012-0378-9>
- Zinqun M (1995) Chinese historical catalogue from 2300 B.C to 1911 A.D. Seismological press, Beijing (In Chinese)

Highlights

- Twin large landslides dammed the same river twice, potentially leading to catastrophic flooding that could have impacted millions downstream.
- First account of site conditions, long-term observed slope displacement, chain of events, deployed early warning system and emergency response, showing how quick and integrated action by local authorities and scientists averted a major disaster.
- The historical deformation trends of the landslide are found using satellite images taken along decades and interferometry of SAR data.

X. Fan · Q. Xu (✉) · **A. Alonso-Rodriguez** · **S. S. Subramanian** · **W. Li** · **G. Zheng** · **X. Dong** · **R. Huang**

State Key Laboratory of Geohazard Prevention and Geoenvironment Protection, Chengdu University of Technology, Chengdu, Sichuan, China
Email: xq-68@qq.com